

Understanding star formation in molecular clouds

II. Signatures of gravitational collapse of IRDCs

N. Schneider^{1,2}, T. Csengeri³, R.S. Klessen^{4,5,6}, P. Tremblin^{7,8}, V. Ossenkopf⁹, N. Peretto¹⁰, R. Simon⁹, S. Bontemps^{1,2}, and C. Federrath^{11,12}

¹ Université Bordeaux, LAB, UMR 5804, 33271 Floirac, France

² CNRS, LAB, UMR 5804, 33271 Floirac, France

³ Max-Planck Institut für Radioastronomie, Auf dem Hügel, Bonn, Germany

⁴ Zentrum für Astronomie der Universität Heidelberg, Inst. für Theor. Astrophysik, Albert-Ueberle Str. 2, 69120 Heidelberg, Germany

⁵ Department of Astronomy and Astrophysics, University of California, Santa Cruz, CA 95064, USA

⁶ Kavli Institute for Particle Astrophysics and Cosmology, Stanford University, SLAC National Accelerator Laboratory, Menlo Park, CA 94025, USA

⁷ Astrophysics Group, University of Exeter, EX4 4QL Exeter, UK

⁸ Maison de la Simulation, CEA-CNRS-INRIA-UPS-UVSQ, USR 3441, CEA Saclay, 91191 Gif-sur-Yvette, France

⁹ I. Physikalisches Institut, Universität zu Köln, Zùlpicher Straße 77, 50937 Köln, Germany

¹⁰ School of Physics and Astronomy, Cardiff University, Queens Buildings, Cardiff CF24 3AA, UK17

¹¹ Monash Centre for Astrophysics, School of Mathematical Sciences, Monash University, VIC 3800, Australia

¹² Research School of Astronomy&Astrophysics, The Australian National University, Canberra, ACT 2611, Australia

September 6, 2022

ABSTRACT

In this paper, we analyze column density and temperature maps derived from *Herschel* dust continuum observations of a sample of prominent, massive infrared dark clouds (IRDCs), i.e., G11.11-0.12, G18.82-0.28, G28.37+0.07, and G28.53-0.25. We disentangle the velocity structure of the clouds using ¹³CO 1→0 and ¹²CO 3→2 data, showing that these IRDCs are the densest regions in massive Giant Molecular Clouds (GMCs) and not isolated features. The probability distribution function (PDF) of column densities for all clouds have a *power-law distribution* over all (high) column densities, regardless of the evolutionary stage of the cloud: G11.11-0.12, G18.82-0.28, and G28.37+0.07 contain (proto)-stars, while G28.53-0.25 shows no signs of star-formation. This is in contrast to the purely lognormal PDFs reported for near/mid-IR extinction maps. Only if we perform PDFs of the column density maps of the *whole* GMC, in which the IRDCs are embedded, we find a lognormal distribution for lower column densities. By comparing the PDF slope and the radial column density profile for three of our clouds, we attribute the power law to the effect of large-scale gravitational collapse and to local free-fall collapse of pre- and protostellar cores for the highest column densities. A significant impact on the cloud properties from radiative feedback is unlikely because the clouds are mostly devoid of star formation. Independently from the PDF analysis, we find infall signatures in the spectral profiles of ¹²CO for G28.37+0.07 and G11.11-0.12, supporting the scenario of gravitational collapse. We are in line with earlier interpretations that see massive IRDCs as the densest regions within GMCs, which may be the progenitors of massive stars or clusters. At least some of them are probably the same features as *ridges* (high-column density regions with $N > 10^{23} \text{ cm}^{-2}$ over small areas) that were defined for nearby IR-bright GMCs. Because IRDCs are only confined to the densest (gravity dominated) cloud regions, the PDF constructed from such a clipped image does not represent the (turbulence dominated) low column density regime of the cloud.

Key words. interstellar medium: clouds

1. Introduction

Infrared dark clouds (IRDCs) were detected as dark, cold ($< 25 \text{ K}$) absorption features with high column density ($N > 10^{22} - 10^{23} \text{ cm}^{-2}$, e.g., Carey et al. 1998, Peretto & Fuller 2010) against the Galactic background at mid-IR wavelengths (Egan et al. 1998). Simon et al. (2006a), Teyssier et al. (2002), and Kainulainen et al. (2011a) showed that some of them are embedded in giant molecular clouds (GMCs), and thus are not isolated features as originally suggested by Egan et al. (1998). Peretto & Fuller (2010) demonstrated on the basis of a large sample (> 10000 clouds) that IRDCs span a large range of masses and sizes with and without star-formation activity. The most massive and

largest IRDCs are proposed to represent the earliest stage of massive star formation (e.g., Rathborne et al. 2006, Nguyen-Luong et al. 2011, Beuther et al. 2013) because they are thought to have not yet started to form stars or are at the verge of star-formation. On the other hand, an increasing number of studies (e.g., Carey et al. 2000, Rathborne et al. 2011, Sakai et al. 2013) now reveal that many of the massive IRDCs show signatures of *active and ongoing (massive) star formation* such as hot core and outflow emission and IR hot spots.

How do these observations fit together? Are IRDCs indeed a special category of molecular clouds/clumps that are dominated by turbulence during their earliest stages of evolution or are they only the densest condensations in massive star-forming clouds and are dominated by gravity as IR-bright clouds? To

Correspondence to: nicola.schneider@obs.u-bordeaux1.fr

Table 1. Coordinates, distance D , and physical parameters of IRDCs, obtained from *Herschel* FIR data, CO data, and near-IR/mid-IR extinction.

Region	l [°]	b [°]	D [kpc]	$\langle N_{dust} \rangle$ [10^{21} cm^{-2}]	$\langle N_{CO,bulk} \rangle$ [10^{21} cm^{-2}]	$\langle N_{CO,cont} \rangle$ [10^{21} cm^{-2}]	M_{dust} [$10^4 M_\odot$]	M_{ext} [$10^4 M_\odot$]	$M_{CO,IRDC}$ [$10^4 M_\odot$]	$M_{CO,GMC}$ [$10^5 M_\odot$]	Σ_{dust} [M_\odot/pc^2]
				(1)	(2)	(3)	(4)	(5)	(6)	(7)	(8)
G11.11-0.12	11.118	-0.118	3.6	22.5	4.6	3.0	8.4	-	2.0	0.5	418
G18.82-0.28	18.822	-0.285	4.8	24.1	12.6	7.1	3.4	1.9	2.9	1.6	448
G28.37+0.07	28.373	0.076	5.0	39.9	20.3	7.7	12.4	6.8	8.3	8.9	741
G28.53-0.25	28.531	-0.251	5.7	25.6	8.8	14.0	9.6	7.4	4.2	1.9	474

(1) average H_2 -column density (N_{dust}) from *Herschel* FIR data within the ellipse defining the IRDC (Simon et al. 2006b).

(2) average H_2 -column density from $^{13}\text{CO } 1\rightarrow 0$ column density (assuming that ^{13}CO is optically thin) with $N(H_2)[\text{cm}^{-2}] = 4.7 \times 10^5 N(^{13}\text{CO})$ in the same ellipse. The velocity range corresponds to the bulk emission of the IRDC. For G11.11-0.12, we used $^{12}\text{CO } 3\rightarrow 2$ data with $N(H_2)[\text{cm}^{-2}] = 2.3 \times N(^{12}\text{CO})$ (Strong et al. 1988) with the ^{12}CO column density $N(^{12}\text{CO})$.

(3) 'contamination' column density from CO data, determined for all velocities lower and higher than that of the IRDC.

(4) Mass $M = N_{dust} 2 m_H \mu A D^2 (\pi/180)^2 [M_\odot]$ with $m_H = 1.67 \times 10^{-24} \text{ g}$, $\mu = 2.3$ (mean atomic weight per molecule), within the area $A [\text{deg}^2]$ of the ellipse defining the IRDC.

(5) Mass of the cloud from near-IR/mid-IR extinction, given in KT and BTK.

(6,7) Mass of the IRDC (6) and associated GMC (7) from CO bulk emission.

(8) Surface density $\Sigma_{dust} = M_{dust}/A$.

address these questions, it is crucial to start with studying the gas reservoir of IRDCs, i.e. the column density structure as the most convenient observable. In particular the probability distribution function (PDF) of column density serves as a key property in characterizing the various physical processes that shape the structure of molecular clouds (see, e.g., Federrath & Klessen 2013 and references therein). Observational studies, based on near-IR extinction or *Herschel* dust column density maps, showed that the PDF of star-forming clouds has a log-normal distribution for low column densities and a power-law tail for higher column densities, where the power-law tail is either interpreted as due to external pressure (Kainulainen et al. 2011b), self-gravity (Froebrich & Rowles 2010; Schneider et al. 2013, 2014) or a combination of both (Tremblin et al. 2014). Numerical simulations (e.g., Padoan et al. 1997; Kritsuk et al. 2007; Federrath et al. 2008a) have shown that supersonic turbulence in isothermal gas (without self-gravity) can reproduce a lognormal distribution. When self-gravity is switched on in the models, a power-law tail develops on the high (column)-density end of the PDF (Klessen 2000; Vazquez-Semadeni et al. 2008; Kritsuk et al. 2011; Federrath & Klessen 2013; Girichidis et al. 2014). The only PDFs reported for IRDCs were either constructed from ALMA dust continuum (G0.253+0.016, Rathborne et al. 2014) or from extinction maps obtained from near- and mid-IR data (Kainulainen & Tan 2013 and Butler, Tan, & Kainulainen 2014, called KT and BTK in the following). The latter are best fitted by lognormal distributions.

In this paper we investigate a sample of four well-known IRDCs from the catalog of Simon et al. (2006b). G11.11-0.12 (the 'snake') lies at a distance of 3.6 kpc and has a linear extent of ~ 30 pc. G18.82-0.28, G28.37+0.07, and G28.53-0.25 are smaller (size of a few pc) and further away (Table 1), and were studied by KT and BTK, who named them Cloud A, C, and D, respectively. The objective of this paper is to show that these IRDCs, that are amongst the most massive in the Galaxy, are dominated by gravity and show the same properties (e.g., average column density, PDF shape, spectral line profiles) as the central cloud regions - called *ridges* (Schneider et al. 2010, Hill et al. 2011, Hennemann et al. 2012) - in IR-bright GMCs.

2. Observations and data analysis

Column density maps from *Herschel*

For this study, we use *Herschel*¹ (Pilbratt et al. 2010) archive data from the Hi-GAL ("*Herschel* Infrared GALactic plane survey", Molinari et al. 2010) program, and reduced the SPIRE (Griffin et al. 2010) and PACS (Poglitsch et al. 2010) data as described in Schneider et al. (2014) by employing the HIPE10 pipeline and scanamorphos v23 (Roussel 2013). The column density and temperature maps are determined from a pixel-to-pixel greybody fit to the 160 μm (PACS), and 250, 350, 500 μm (SPIRE) wavelengths (maps with 36'' resolution). All *Herschel* maps have an absolute flux calibration, using the Planck-corrections from the ZEROPOINTCORRECTION task in HIPE10 for SPIRE and IRAS maps for PACS. For the SED fit, we fix the specific dust opacity per unit mass (dust+gas) approximated by the power law $\kappa_\nu = 0.1 (\nu/1000\text{GHz})^\beta \text{ cm}^2/\text{g}$ and $\beta=2$, and leave the dust temperature and column density as free parameters (see Schneider et al. (2014) for further details). We estimate the final uncertainties in the column density maps to be around $\sim 30\text{--}50\%$, mainly arising from the uncertainty in the assumed form of the opacity law and possible temperature gradients along the line-of-sight (Russeil et al. 2013, Roy et al. 2013).

Molecular line data: $^{13}\text{CO } 1\rightarrow 0$ and $^{12}\text{CO } 3\rightarrow 2$

Data cubes of $^{13}\text{CO } 1\rightarrow 0$ (110.2 GHz) emission were taken from the Galactic Ring Survey archive (GRS), a survey covering the first Galactic quadrant (Jackson et al. 2006), obtained with the Five Colleges Radio Astronomy Observatory (FCRAO). The angular resolution is $\sim 45''$ at a velocity resolution of 0.21 km s^{-1} . $^{12}\text{CO } 3\rightarrow 2$ (345.8 GHz) data (angular resolution of $14''$ and velocity resolution of 1 km s^{-1}) were obtained from the JCMT/COHRS archive (Dempsey et al. 2013). Both CO data sets are given on a main beam brightness temperature scale.

ATLASGAL

The ATLASGAL survey (Schuller et al. 2009) imaged 420 deg² of the Galactic plane ($l=\pm 60^\circ$, $b=\pm 1.5^\circ$) at a 19.2'' spatial resolution at 870 μm with the LABOCA camera Siringo et al. (2009) on the APEX Telescope. The data, together with the catalog of

¹ *Herschel* is an ESA space observatory with science instruments provided by European-led Principal Investigator consortia and with important participation from NASA.

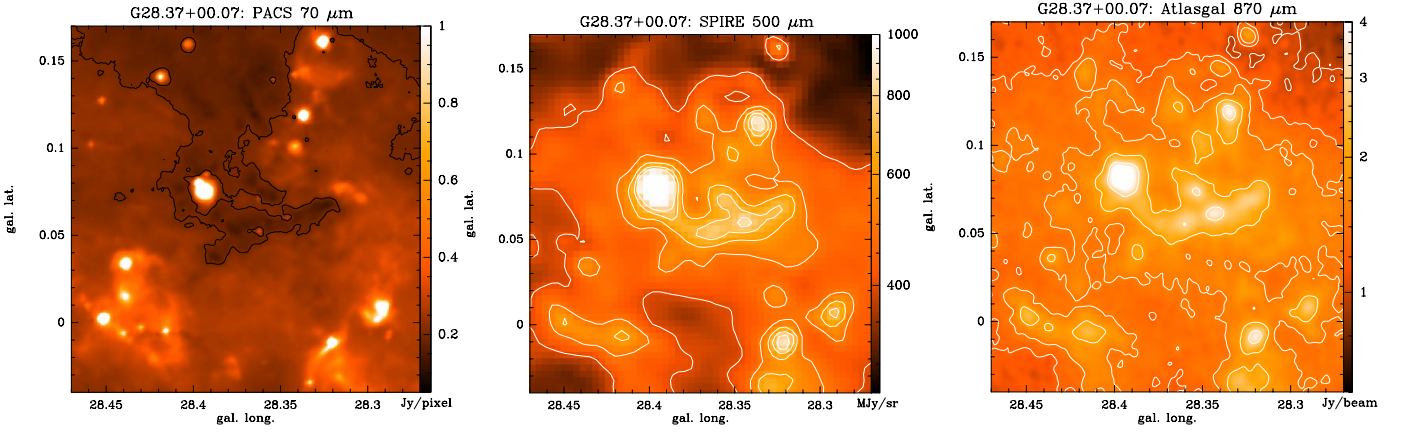


Fig. 1. PACS 70 μm map (left, 11'' resolution), SPIRE 500 μm map (middle, 36'' resolution), and ATLASGAL 870 μm map (right, 23'' resolution) of G28.37+0.07. The central dark feature in the PACS image is the IRDC, appearing bright at longer wavelengths (SPIRE and ATLASGAL).

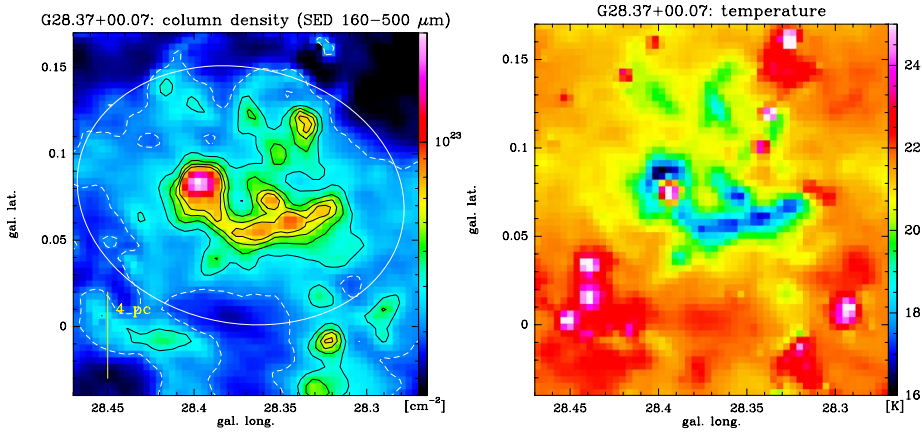


Fig. 2. Left: H_2 column density map from an SED fit to *Herschel* fluxes at 160–500 μm . The black contours indicate the levels $N_{\text{dust}}=4$ to $7 \times 10^{22} \text{ cm}^{-2}$ in steps of 10^{22} cm^{-2} , the white dashed contour outlines the approximate completeness level, and the white ellipse is taken from Simon et al. (2006b), defining the IRDC.

Right: Temperature map of G28.37+0.07.

compact sources, is presented in Csengeri et al. (2014). Here, we make use of the publicly available ATLASGAL data². Ground-based bolometer observations intrinsically filter emission from larger scales when removing the correlated noise during the data reduction. In the original LABOCA observations, the low-level emission is thus filtered out, so that only the densest cloud regions are visible. This diffuse emission is recovered from low angular resolution all-sky surveys of Planck/HFI following the method of Weiss et al. (2001). This combined dataset therefore is sensitive to the cold dust at all spatial scales (for details see Csengeri et al. in prep) and was used to select the regions corresponding to the IRDCs. For display reasons, we slightly smoothed the data to 23'' angular resolution. The sensitivity of the data is dominated by the noise level of the ATLASGAL survey, which in these regions is $\sim 60 \text{ mJy/beam}$.

3. Results and discussion

In this section we show as a representative case all continuum and molecular line data for G28.37+0.07 (Cloud C), which was studied in Simon et al. (2006b), KT, and BTK. Maps for the other three clouds are shown in Appendix A.

3.1. G28.37+0.07 with *Herschel* and ATLASGAL

Figure 1 displays G28.37+0.07 as a *dark feature* in the 70 μm PACS map but with an *emission peak* at $l=28.396^\circ$, $b=0.081^\circ$. The cloud is overall bright at 500 μm and 870 μm , but also at 8 μm (Carey et al. 2000, BTK). It corresponds to an IRAS source (IRAS18402-403), and contains massive protostellar cores (Zhang et al. 2009), and is thus most likely a protocluster. Because this peak is prominent also at longer wavelengths, the protocluster is still embedded in a dense, cold, molecular envelope. In particular the 500 and 870 μm maps, tracing the large-scale distribution of *cold*, molecular gas, show that the IRDC is not an isolated feature. This becomes also obvious in the column density and temperature maps (Fig. 2), where this central region is outlined by low temperatures around 16 to 19 K (except for the locally heated protostellar environment), and column densities of $6 \times 10^{22} \text{ cm}^{-2}$ to a few 10^{23} cm^{-2} . Comparing our column density maps with those of KT and BTK shows an overall very good correspondence, except for the high column density peak that is missing in the latter studies because (i) there is extinction saturation, i.e., mid-IR foreground emission is as bright as the emission toward the cloud, and (ii) it is a bright 8 μm region: the densest part of G28.37+0.07 is emitting strongly at 8 μm , so it does not appear as an extinction feature. Therefore recover-

² <http://atlasgal.mpifr-bonn.mpg.de/>

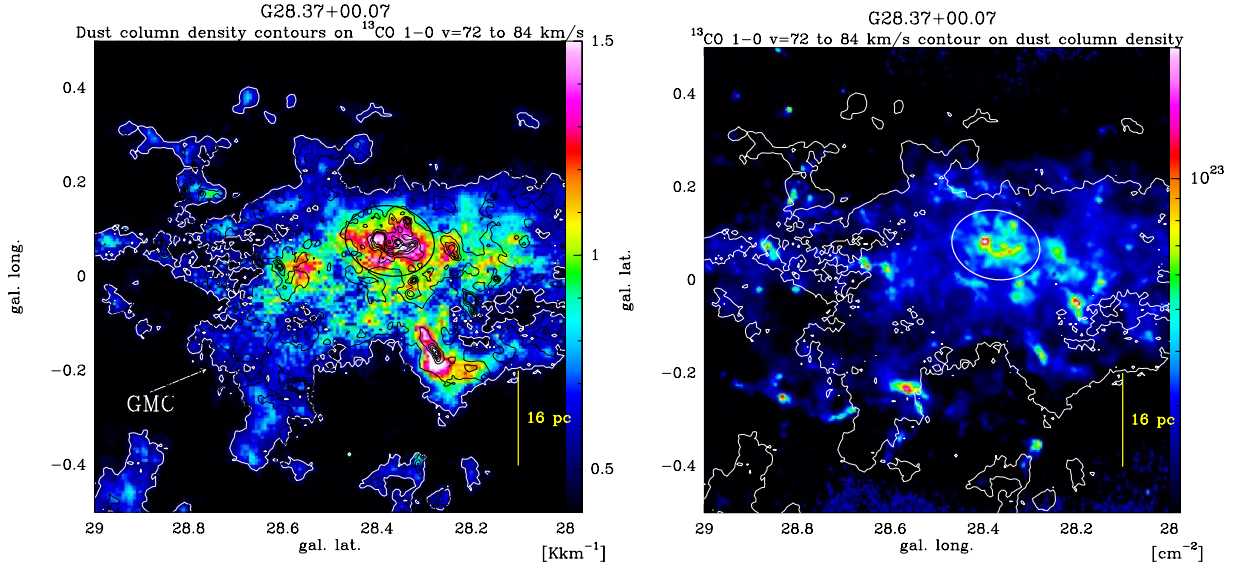


Fig. 3. Left: Line integrated ^{13}CO 1 \rightarrow 0 emission in color scale between $v=72$ and 84 km s^{-1} , the velocity range of the bulk emission of the IRDC and the associated GMC. The white contour indicates the 0.5 K km s^{-1} level that defines roughly the extent of the GMC and that was used for the mass estimation. The *Herschel* column density is overlaid as black contours (levels 2 to $6\times 10^{22}\text{ cm}^{-2}$ in steps of 10^{22} cm^{-2}) and the IRDC is outlined by an ellipse (Simon et al. 2006b). **Right:** *Herschel* column density in color scale with a white contour (0.5 K km s^{-1} level) of ^{13}CO 1 \rightarrow 0 emission outlining the GMC. The pixels inside this contour were used to make the dust column density PDF of the GMC.

ing the column density structure from an extinction map at these positions is impossible (Peretto & Fuller 2010).

3.2. G28.37+0.07 in ^{13}CO 1-0 emission

3.2.1. The IRDC as part of a GMC

In order to identify the exact velocity range of G28.37+0.07, we followed the method outlined in Simon et al. (2006b) to use the GRS ^{13}CO 1 \rightarrow 0 data to establish a morphological match between the *Herschel* column density map and ^{13}CO emission. Simon et al. (2006b) already listed this source with a velocity (v_{lsr}) of 78.6 km s^{-1} and a velocity dispersion of 8.3 km s^{-1} . Figure 3 shows the large-scale velocity integrated (72 to 84 km s^{-1}) ^{13}CO map with the dust column density overlaid as contours (and vice versa). The overall correspondence between the two tracers is good, the two most prominent peaks in ^{13}CO emission correlate well with contours of dust column density, indicating that most of the dust seen with *Herschel* indeed comes from gas of the molecular cloud at that velocity range, i.e., the bulk emission of the cloud. In particular the prominent peak at 500 and $870\text{ }\mu\text{m}$ emission and column density (Fig. 1), shows up as a peak in ^{13}CO (and N_2H^+ 1 \rightarrow 0 at the same velocity, Tackenberg et al. 2014), so that this high-column density clump is clearly an intrinsic part of the IRDC. All ^{13}CO emission outside this velocity range is due to diffuse emission and/or clouds along the line-of-sight (see column 3 in Table 1). This large-scale comparison shows that G28.37+0.07 is a part of a much larger molecular cloud complex. The same is true for the other clouds in this study. Appendix A shows a ^{12}CO 3 \rightarrow 2 map of G11.11-0.12 and ^{13}CO 1 \rightarrow 0 maps of G18.82-00.28 and G28.53-00.25. Because of the spatial limit of the COHRS ^{12}CO survey, the GMC associated with G11.11-0.12 (Fig. A.2) is not fully comprised toward lower galactic latitudes. However, G11.11-0.12 is clearly not an isolated feature but forms the densest region within this GMC that has a mass of at least $0.5\times 10^5\text{ M}_\odot$ (Table 1). G18.82-00.28 and G28.53-00.25 (Figs. A.4 and A.6) are part of more massive

clouds ($\sim 2\times 10^5\text{ M}_\odot$) that were fully included in the GRS ^{13}CO survey. We are thus in line with earlier findings (e.g., Carey et al. 2000, Simon et al. 2006a, Teyssier et al. 2002) that see IRDCs as an intrinsic part of a larger molecular cloud.

3.2.2. Mass determination and link to IR-bright GMCs

Integrating all ^{13}CO emission above $\sim 0.5\text{ K km s}^{-1}$ leads to a total mass of $\sim 10^6\text{ M}_\odot$ (Table 1) and an equivalent radius of $\sim 40\text{ pc}$ for the GMC. The IRDC G28.37+0.07 occupies only a small spatial fraction within the GMC, has a high average and peak column density ($\sim 4\times 10^{22}\text{ cm}^{-2}$ and $\sim 3\times 10^{23}\text{ cm}^{-2}$, respectively), and a high surface density ($\Sigma_{\text{dust}} \sim 740\text{ M}_\odot\text{ pc}^{-2}$). It thus shows the characteristics of *ridges* that were defined as the central regions within a GMC with column densities above $\sim 10^{23}\text{ cm}^{-2}$ at temperatures below 20 K for the IR-bright cloud Vela C (Hill et al. 2011) and the DR21 ridge³ (Schneider et al. 2010, Hennemann et al. 2012).

We also estimated the line-of-sight (LOS) contribution from ^{13}CO emission and found that the average H_2 column density in the velocity ranges *outside* the bulk emission, within the ellipse is $\langle N_{\text{CO,cont}} \rangle = 7.7\times 10^{21}\text{ cm}^{-2}$, a significant value, compared to $\langle N_{\text{CO,bulk}} \rangle$ of $20.3\times 10^{21}\text{ cm}^{-2}$ for the cloud itself. The $\text{HI}+\text{H}_2$ column density $\langle N_{\text{dust}} \rangle$ determined from the *Herschel* map is $\sim 40\times 10^{21}\text{ cm}^{-2}$, and thus twice as high as $\langle N_{\text{CO,bulk}} \rangle$. If ^{13}CO becomes optically thick and/or freezes out in the highest density regions, it underestimates the H_2 column density. On the other hand, the *Herschel* column density map is affected by line-of-sight contamination and thus overestimates the H_2 column density. Considering these effects and the uncertainties of the methods, a factor of 2 disagreement between the column density determined from CO and dust is acceptable. The total lower limit of the mass derived using ^{13}CO of the bulk emission is 8.3×10^4

³ Note that the DR21 ridge itself is an IRDC (Marston et al. 2004), and that the IRDC G035.39-0.33 in W48 was already qualified as a *ridge* (Nguyen-Luong et al. 2011) with the same physical properties.

M_{\odot} , comparable to the mass calculated from extinction, and 33% lower than the *Herschel* mass. Because the total mass of a cloud is mainly determined by its lower-density gas on a larger spatial distribution (visible in Fig. 3), saturation at high densities has less of an impact on the total mass estimate.

4. Probability distribution functions of IRDCs

The PDFs⁴ of dust column density for the IRDC G28.37+0.07 and its associated GMC are shown in Fig. 4, the ones for G11.11-0.12, G18.82-0.28, and G28.53-0.25 in Appendix B. To be consistent with other studies, we express the PDF in visual extinction A_V using the conversion $N(H_2)/A_V = 0.94 \times 10^{21} \text{ cm}^{-2} \text{ mag}^{-1}$ (Bohlin et al. 1978).

All PDFs are sampled with a binsize of 0.15 (in η) using maps of a grid of 14'' (see Schneider et al. 2014 for more details on sampling effects). They are constructed from pixels above the approximate completeness limit within the ellipses defining the IRDC. This level was obtained from the column density maps (e.g., Fig. 2) where we determined the contour level (indicated by a white dashed line) above the majority of pixels is still found within the ellipse defining the IRDC. Below this contour, the map is undersampled, which leads to a pixel distribution that is not representative and can create an artificial fall-off of the PDF for lower column densities (which should not be confused with the peak of a lognormal PDF).

The PDF of the IRDC alone obtained in this way – as well as the PDFs for the other IRDC clouds (see Fig. B.1) – is consistent with a pure *power-law distribution*. In contrast, the PDF of the whole GMC (Fig. 4, bottom) in which the IRDC is embedded indeed shows a lognormal part plus a power-law tail, similar to what was found for star-forming clouds (e.g., Kainulainen et al. 2011b, Schneider et al. 2013). The reason for the missing lognormal part in the PDF of the IRDC alone is that the cloud is not sampled down to the lowest A_V -ranges and a PDF from an image where the low column density pixels are ignored is just composed of a power-law distribution (Schneider et al. 2014).

In order to illustrate this cropping effect, we made PDFs from pixels above different A_V -thresholds for the whole GMC (Fig. 3) using the *Herschel* dust column density map (see right panel of Fig. 3). Figure 5 shows how the PDF changes from a distribution that can be described by a lognormal plus power-law distribution (for pixels above $A_V = 12$) into a purely power-law distribution (for pixels above $A_V = 20$). Note that the curves 'shift' due to different normalizations (the area/number of pixels decreases with increasing A_V -level). We emphasize that the contour outlining the GMC still comprises higher column density gas ($A_V > 10$) which is well above the threshold of typically $A_V = 1$ or 2 (e.g., Lada et al. 2010) that is commonly used to 'define' the extent of a molecular cloud. But the dust continuum map suffers from line-of-sight contamination on a high level of at least $A_V \sim 8$ –10 because (i) this is the value at the map borders outside of the GMC (Fig. 5), and (ii) corresponds also to the H_2 column density derived from ^{13}CO adding all emission outside of the bulk emission of the GMC (Sec. 3.2).

In any case, the main point of this exercise is to demonstrate that the PDF of the IRDC (Fig. 4, top), can be fitted by a pure power law above A_V -values of ~ 30 . This PDF can directly be compared to the one shown in BTK (their Fig. 3, left panel)

⁴ We define $\eta \equiv \ln(N/\langle N \rangle)$ as the natural logarithm of the column density N , divided by the mean column density $\langle N \rangle$, and the quantity $p_{\eta}(\eta)$ then corresponds to the PDF of η with the normalization $\int_{-\infty}^{+\infty} p_{\eta} d\eta = \int_0^{+\infty} p_N dN = 1$ (see Schneider et al. 2014 for details).

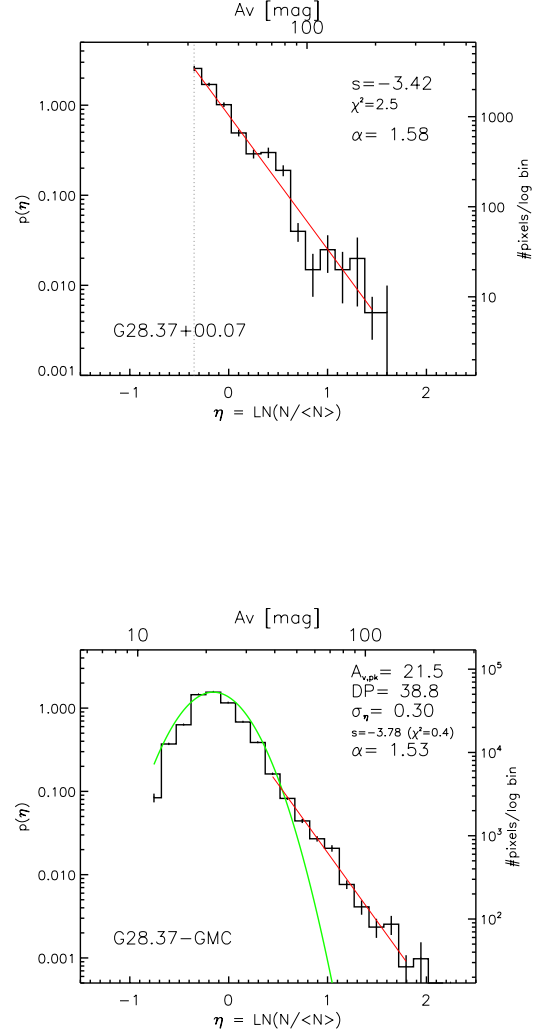


Fig. 4. PDFs of G28.37+0.07 and its associated GMC, derived from the *Herschel* column density map. The upper panel shows the PDF of the IRDC, only from the pixels inside the ellipse shown in Fig. 2, the lower panel the PDF obtained for the whole GMC (all pixels inside the contour indicated in Fig. 3, right). The left y-axis gives the normalised probability $p(\eta)$, the right y-axis the number of pixels per log bin. The upper x-axis is the visual extinction and the lower x-axis the logarithm of the normalised column density. The green curve shows a lognormal fit to the PDF from the GMC. The red line indicates a power-law fit to the high column density tail with the slope s and the exponent α of an equivalent spherical density distribution $\rho(r) \propto r^{-\alpha}$ indicated in the panel. The dashed line in the upper panel indicates the completeness level, the PDF left of this line is incomplete due to undersampling.

that shows a broad PDF and an apparent peak at A_V around 8, and which is fitted by a lognormal distribution with a width of $\sigma = 1.7$. Their PDF is not complete but moreover clipped (see above) because it represents only the cloud center. In addition, the highest column density pixels (above $A_V \sim 100$) are missing because they were masked out.

In order to exclude a possible lognormal distribution for our observed PDF of the IRDC, we performed a 2-sample

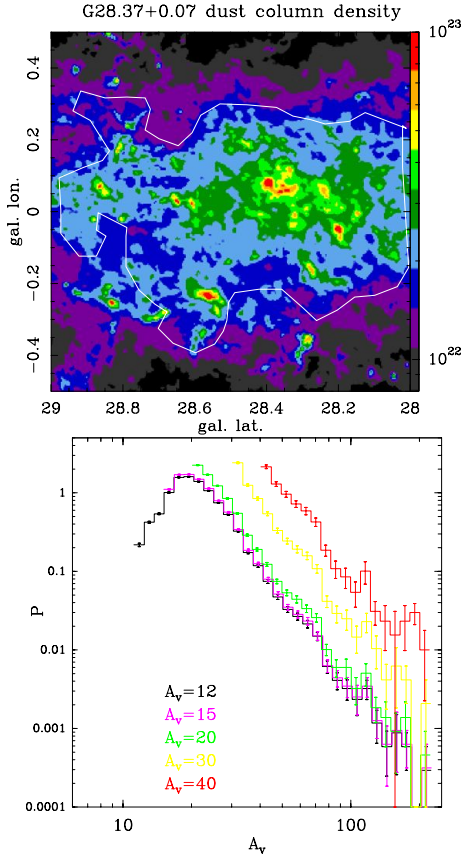


Fig. 5. Top: H_2 column density from dust continuum with the 0.5 K km/s contour (white), roughly outlining the GMC in which G28.37+0.07 is embedded. **Bottom:** PDFs of the GMC, derived from the dust column density map from the left above different A_V -thresholds (indicated with different colors and given in the panel).

Kolmogorow-Smirnov (KS)-test, comparing our distribution with a set of pure lognormal distributions with different widths ($\sigma=0.2$ to 1.7) and normalizations (see Appendix C for details). The probabilities p in all cases are very low so that we exclude the possibility that our observed PDF is purely lognormal. We also made a KS-test using our PDF of the IRDC (Fig. 4, top), but including the data points left of the completeness level and ignoring the data points above $A_V \sim 100$. The 2-sample KS-test with the synthetic PDFs equally shows also small values for p , i.e., between 0.01 for $\sigma=1.7$ to 1.6×10^{-4} for $\sigma=0.2$.

In Appendix B, we show the PDFs of the other IRDCs (alone and including the embedding GMC). The result is the same as for G28.37+0.07, i.e., a lognormal plus power-law tail for the GMC and a power-law distribution for the IRDC. For G28.53-0.25, there is an indication for a lognormal distribution below $A_V \sim 30$. Note, however, that the PDFs of the GMC are less reliable because effects of line-of-sight contamination become more important and can lead to a change in slope for the power-law tail (Schneider et al. 2014).

5. Global and local gravitational collapse of IRDCs

The power-law distribution we find for all PDFs of the IRDCs in our sample is in accordance with the power-law tails found for IR-bright clouds (Lombardi et al. 2008; Kainulainen et al. 2009; Hill et al. 2011; Schneider et al. 2012, 2013, 2014; Russeil et

al. 2013; Tremblin et al. 2014; Alves de Oliveira et al. 2014). In these studies, a clear turnover from a lognormal distribution for low column densities (typically from $A_V < 1$ up to A_V of a few magnitudes) into a power-law tail was observed. Self-gravity as the dominating (over pressure and magnetic fields) process to form this power-law tail was advocated by numerical models (Klessen 2000, Federrath et al. 2008b, Kritsuk et al. 2011) and observationally supported by Froebrich & Rowles (2010) and Schneider et al. (2013). Recently, Rathborne et al. (2014) obtained a PDF from ALMA continuum data for the IRDC G0.253+0.016 in the Central Molecular Zone (CMZ) which has a lognormal shape and some excess at highest column densities they attribute to self-gravity within the most massive cores. In the following, we will present additional evidence from radial column density profiles and molecular line observations that IRDCs are in gravitational collapse, which is reflected in the power-law distribution of the column density.

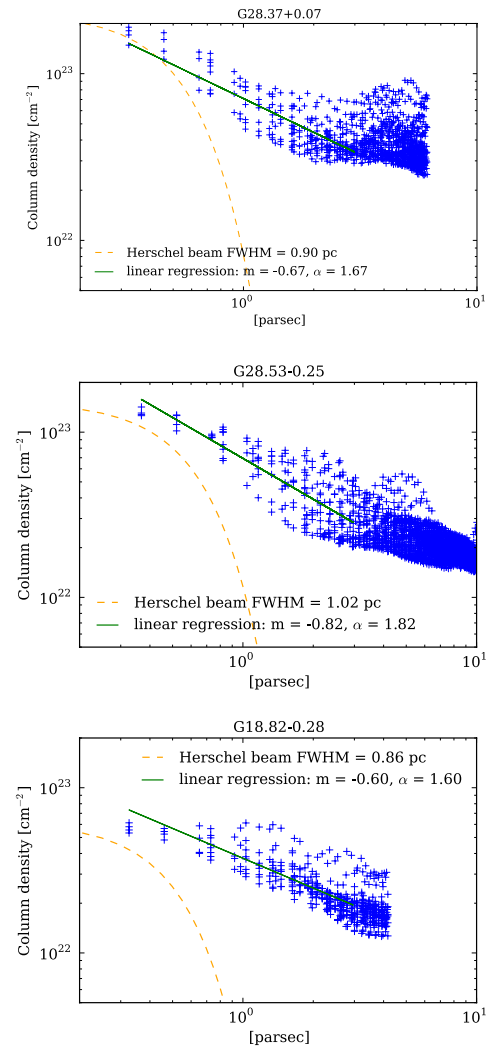


Fig. 6. Radial column density profile for G28.37+0.07, G28.53-0.25, and G18.82-0.28. Each cross in the panels represents one pixel value in the map. The x-axis gives the distance to the center of the ellipse (x-axis). The dashed yellow line indicates the Herschel beam (Gaussian profile with a FWHM of $36''$ displayed in log-log format). The exponent α was deduced from fitting the column density profile ($N \propto r^{1-\alpha}$).

Table 2. Exponents α and their errors $\Delta\alpha$, assuming a spherical density distribution $\rho(r) \propto r^{-\alpha}$, derived from the slope s of the power-law distribution from the PDF (column 2) and from the column density profiles (column 3).

Region	α (PDF)	$\Delta\alpha$ (PDF)	α (profile)	$\Delta\alpha$ (profile)
G28.37+0.07	1.58	0.07	1.67	0.02
G28.53-0.25	2.02	0.14	1.82	0.06
G18.82-0.28	1.49	0.06	1.60	0.03

5.1. The link between the PDF power-law tail and the column density profile

Provided that the power-law distribution of the PDF is only due to gravity, and if we assume spherical symmetry, the power-law slope s of the PDF is related to the exponent α of a radial density profile according to $\rho(r) \propto r^{-\alpha}$ and $\alpha = -2/s + 1$ (Federrath & Klessen 2013). For the PDFs of the IRDCs in our sample (Fig. 4 and B.1), we obtain values between $\alpha \sim 1.5$ and 2.5 . This is consistent with a structure dominated by *self-gravity*, i.e. local free-fall of individual cores and clumps and global collapse (Girichidis et al. 2014, Schneider et al. 2014). To which extent the variations in the slope can be attributed to the evolutionary state of the cloud is not clear. As was shown in simulations (Ballesteros-Paredes et al. 2011, Federrath & Klessen 2013), the power-law flattens with time/increasing star formation efficiency. In our small sample of IRDCs, however, the low value of α points towards an early state in cloud evolution.

In order to derive a PDF-independent value for the exponent α , we fitted the radial column density profiles of G28.37+0.07, G28.53-0.25, and G18.82-0.28 (Fig. 6). From our sample, only these sources can roughly be approximated as “spherical”, G11.11-0.12 is too filamentary. Assuming again spherical geometry, the column density N can be expressed as $N \propto \rho(r) \times r \propto r^{1-\alpha}$, thus the exponents α from the PDF and the column density profile should correspond. Within the error bars, this is approximately the case (see Table 5), we obtain from the column density profile $\alpha=1.58, 2.02, 1.49$ for G28.37+0.07, G28.53-0.25, and G18.82-0.28, respectively, compared to $\alpha=1.67, 1.82, 1.60$, deduced from the PDF. Interestingly, the pixels that constitute the power law in the PDF are distributed homogeneously without breaks across all column densities in the radial profile, indicating that we most likely observe a global feature, i.e., a *large-scale global collapse of the IRDC*. In the next section, we demonstrate that complementary molecular line data indeed point towards such a scenario for our IRDCs.

5.2. Collapse signatures in molecular line profiles

The shape of molecular line profiles allows to disentangle various dynamic processes such as outflows, rotation, and infall, within a molecular cloud/clump/core. Gas inward motions caused by gravity in regions of star-formation lead to a self-absorbed emission line profile (‘double-peak’ or ‘P-Cygni profile’) of an optically thick line. An optically thin line must then peak in the self-absorbed dip in order to exclude the possibility of several line components and rotation. Simple early models (see, e.g., Myers et al. 1996 and references therein) are based on a gravitationally collapsing isothermal sphere and predict a

‘blue asymmetry’, i.e., with increasing infall speed, the blue peak in the double-peak profile becomes brighter than the red one. However, recently Smith et al. (2012, 2013) showed that collapsing *embedded* cores show more complex line profiles due to the contribution of the enclosing filament.

In any case, there are a number of examples where infall signatures in spectral profiles have been detected and successfully modelled, mostly for isolated low-mass cores (e.g., Walker et al. 1994, Tafalla et al. 2002) and high-mass cores (e.g., Csengeri et al. 2011). Gravitational collapse of a whole filament on a scale of a few pc was seen for the DR21 ridge (Schneider et al. 2010) and Serpens-South (Kirk et al. 2013). Global collapse of IRDCs was suggested for SDC335 (Peretto et al. 2013), G79.3+0.3 (Carey et al. 2000), and G32.03+0.05 (Battersby et al., priv. comm.).

For the IRDCs in our sample, we use the ^{12}CO 3 \rightarrow 2 line from the COHRS archive as an optically thick tracer, and ^{13}CO 1 \rightarrow 0 from the GRS as the optically thin line. For better comparison, we smoothed the ^{12}CO data to the resolution of the ^{13}CO data (45’). Both CO-data sets together are only available for G28.37+0.07. For this source, we show in Fig. 7 the velocity integrated ^{12}CO map and spectra from selected positions, i.e., the strongest submm continuum sources from ATLASGAL (Contreras et al. 2013, Csengeri et al. 2014) and two positions off-source but within the cloud. The continuum sources were also observed in the optically thin N_2H^+ 1 \rightarrow 0 line at 93.173 GHz with a velocity resolution of 0.2 km s $^{-1}$ (Tackenberg et al. 2014), and the center velocities reported in their Table 3 are indicated as a dashed blue line in Fig. 7. Note that the same velocity of sources 2 and 6 are also derived by Shipman et al. (2014) based on pointed observations of optically thin lines such as N_2H^+ and C^{17}O , using *Herschel* and APEX.

It becomes obvious that the ^{13}CO 1 \rightarrow 0 line consists of several components, but there is no ‘double-peak’ feature and the center velocity of the main Gaussian corresponds very well to the velocities determined with N_2H^+ , so that ^{13}CO emission is optically thin or only moderately optically thick. Most importantly, the main ^{13}CO line peaks in the gap of a double-peaked ^{12}CO line, best visible for sources 1 and 4. Source 2 (most likely a protocluster, see Sec. 3.1) is more complex with several line components, associated with CH_3OH and H_2O masers (Pillai et al. 2006; Wang et al. 2008, 2014) and harbours a hot-core (Zhang et al. 2009). Note that some sources – in particular source 1 for velocities lower than ~ 70 km s $^{-1}$ – show broad wings that possibly indicate outflow emission from the protostellar object. This becomes more evident when the on-source ^{12}CO spectra are compared to two spectra (indicated by offset $-720''$, $220''$ and $-1000''$, $220''$ in Fig. 7) that are located off source but still within the IRDC. These also show the self-absorption dip but no prominent wings. Though it is out of the scope of the paper to go into more detail for outflows, it is important to recognize those as indicators for star formation.

Though ^{12}CO is not the best tracer for infall signatures – HCO^+ or HCN are better suited because they show a clearer profile (Schneider et al. 2010) – the general behaviour is the same. Since we can exclude rather safely by using the ^{13}CO spectra and the N_2H^+ velocity information the possibility that the double-peak profile of ^{12}CO is due to several line components, the most likely explanation is that we observe inward motions of gas. *Local infall* on the pre- and protostellar sources is seen in H_2O observations (Shipman et al. 2014) of source 2 and source 6 (labeled G28-MM and G28-NH $_3$ in Shipman et al. 2014), where the water line appears in absorption and is systematically redshifted relative to the systemic velocity of the clump. However, comparing ^{12}CO and ^{13}CO spectra across the whole IRDC (the two

⁵ Note that these are lower limits for α because the power-law slope steepens due to line-of-sight contamination (Schneider et al. 2014).

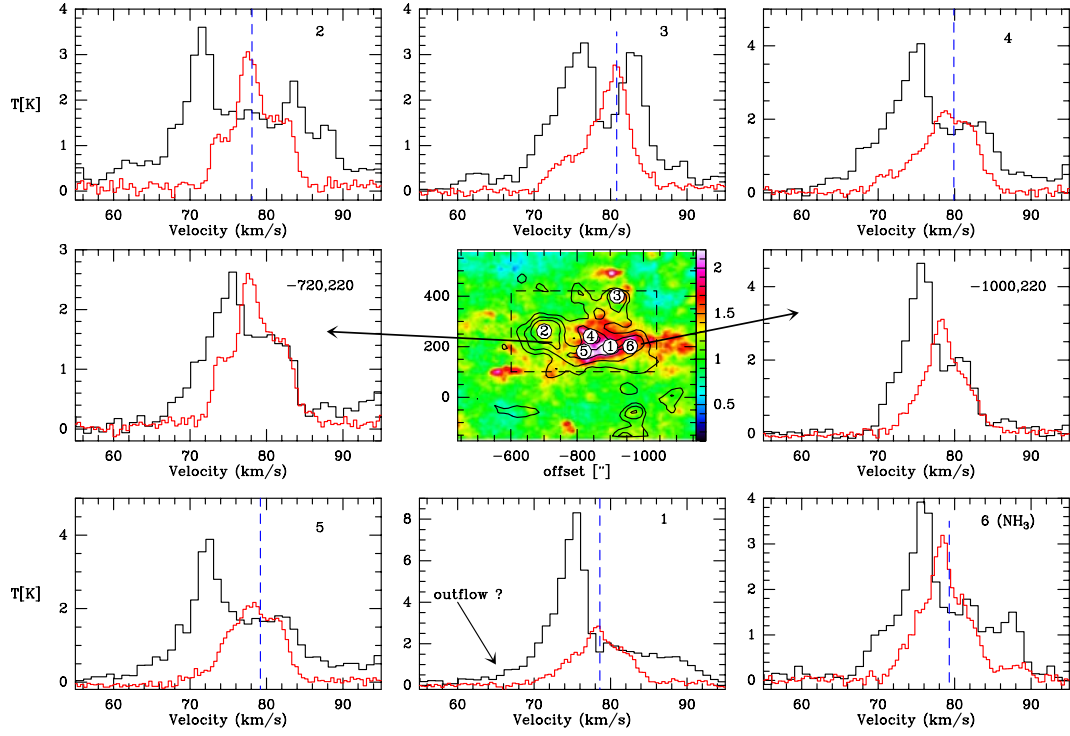


Fig. 7. The middle panel shows in color the line integrated ^{12}CO 3 \rightarrow 2 emission (between 72 and 84 km s $^{-1}$) of G28.37+0.07. The dust column density from *Herschel* is overlaid as black contours (levels 4, 5, 7 10^{22} cm $^{-2}$). The dashed lines outline the area displayed in Fig. 8, and the numbering from 1 to 6 indicates the position of submm-continuum sources seen with ATLASGAL and subsequently observed in N_2H^+ (Tackenberg et al. 2014). The ^{12}CO 3 \rightarrow 2 (black) and ^{13}CO 1 \rightarrow 0 (red) spectra at these positions are displayed in the panels around. Additionally, we show spectra from two positions (indicated by arrows) off the sources. The blue dashed line denotes the center velocity of the N_2H^+ line.

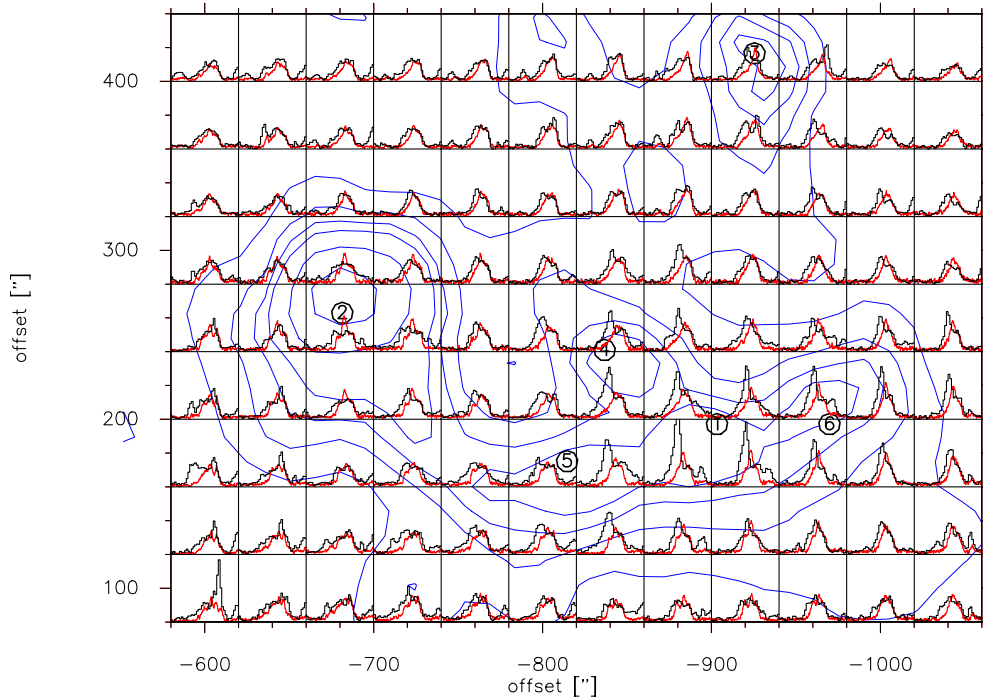


Fig. 8. Spectra of ^{12}CO 3 \rightarrow 2 (black) and ^{13}CO 1 \rightarrow 0 (red) emission in the velocity range 55 to 95 km s $^{-1}$ and temperature range 0.2 to 6 K. The area corresponds to the center region of the IRDC G28.37+0.07, outlined in Fig. 7. The dust column density from *Herschel* is overlaid as blue contours (levels 4, 5, 7, 10, 16 10^{22} cm $^{-2}$), and the numbering from 1 to 6 indicates the position of submm-continuum sources labeled using ATLASGAL and subsequently observed in N_2H^+ (Tackenberg et al. 2014).

off-source spectra in Fig. 7, and Fig. 8) shows that the double-peak profiles extend well beyond the source positions and are found basically everywhere inside the blue contours, outlining the IRDC. We thus propose that the whole IRDC is in *global collapse*.

In appendix D, we show that infall ^{12}CO profiles are also observed for G11.11-0.12. Because we have no complementary ^{13}CO data, the global collapse scenario there is more tentative. However, single pointings in H_2O in G11.11-0.12 (Shipman et al. 2014) already show infall signatures similar to G28.37+0.07, so that we conclude that global collapse could probably be a feature shared by all *massive* IRDCs that are embedded in GMCs. Higher angular resolution molecular line observations using, e.g. HCO^+ or HCN and the optically thin isotopologues H^{13}CO^+ or H^{13}CN as line tracers, are required to investigate in more detail this scenario.

6. Summary and Conclusions

Our study using *Herschel*, ATLASGAL and ^{12}CO and ^{13}CO molecular data shows that massive IRDCs are embedded in more extended molecular clouds and have similar physical properties (peak and average column density, surface density) as *ridges*, i.e., the densest, central regions of GMCs. The PDFs for all four IRDCs obtained from *Herschel* dust column density maps show a power-law distribution, which we interpret as arising from gravitational contraction. There is no lognormal part in the PDF because the PDF is constructed from a cropped image, focussing on the densest region within the GMC. On the other hand, the PDF of the associated GMC shows a lognormal form for lower column densities and a power law for high densities.

We give two additional and independent arguments for the dominance of self-gravity for the IRDCs presented in this paper. First, fitting the radial column density profiles leads to similar exponents $\alpha=1.70\pm0.07$ as derived from the slope of the PDF power-law distribution ($\alpha=1.70\pm0.16$), and is consistent with self-gravity ($\alpha=1.5$ to 2 assuming a spherical density distribution). Second, molecular line profiles of the optically thick ^{12}CO 3 \rightarrow 2 line show self-absorption at the velocity of the bulk emission of the cloud, indicating locally infalling gas on proto- and prestellar cores but also on the global IRDC scale.

The self-gravitating scenario on all scales is consistent to what is found in numerical models. Just to list a few, Ballesteros-Paredes et al. (2011), Kritsuk et al. (2011), Federrath & Klessen (2013), Girichidis et al. (2014), Ward et al. (2014) obtain a lognormal+power law tail PDF (density or column density) for their simulations including self-gravity and turbulence but without external pressure (such as radiative feedback). First, turbulence creates a self-similar structure of the gas that is well represented by a purely lognormal PDF. As soon as self-gravity is switched on and collapse proceeds for some time, the hierarchical structure in clouds is affected and the (column) density PDF departs from a lognormal and forms a power-law tail. Studies focussing on the *spatial* cloud structure, using power-spectra or the Δ -variance (see Schneider et al. 2011 and references therein) also show that molecular clouds lose their hierarchical structure and show characteristic scales as soon as star-formation sets in. Federrath & Klessen (2013, Fig. 4) link the change of the slope of the PDF to the star-formation efficiency (SFE). Their simulations are consistent with our observations. The PDFs of the IRDCs we present in this paper all show a power-law distribution with similar slopes, regardless of their evolutionary states: G18.82-0.28 and G28.37+0.07 show bright peaks at 70 μm , and in G11.11-0.12 the presence of IR-bright protostars was demon-

strated (Henning et al. 2010). G28.53-0.25 is in a very early stage because it contains no (F)IR-bright peaks. Despite its youth, this cloud shows a power law distribution over all column densities. Given the uncertainties in the column-density PDFs, the slope differences are marginal and it is difficult to distinguish an SFE of 5% from 20% for most parameter sets of the simulations (note that the PDFs from simulations differ from the ones of observations, because they are averages over all three lines of sight from different directions). Given that the IRDCs of our sample are all in a collapsing state and most of them have already started forming stars, they might well have local SFE of $\sim 5\%$ in agreement with the models shown in Federrath & Klessen (2013).

Acknowledgements. We thank P. Girichidis for discussions on collapse scenarios. N.S. and S.B. acknowledge support by the ANR-11-BS56-010 “STARFICH”. N.S., V.O., and R.S.K. acknowledge funding from the DFG priority program SPP 1573 “Physics of the ISM” (project number OS177/2-1 and KL 1358/19-1). R.S.K. acknowledges subsidies from the collaborative research project SFB 881 (“The Milky Way System”, subprojects B1, B2, and B5), and support from the ERC Framework Programme FP7/2007-2013 via the ERC Advanced Grant STARLIGHT (project number 339177). R.S.K. thanks for the warm hospitality at the Department of Astronomy and Astrophysics at the University of California at Santa Cruz and the Kavli Institute for Particle Astrophysics and Cosmology at Stanford University and during a sabbatical stay in 2014 and 2015. T.Cs. acknowledges financial support for the ERC Advanced Grant GLOSTAR under contract no. 247078.

References

- Alves de Oliveira, C., Schneider, N., Merin, B., et al., 2014, A&A568, 98
- Ballesteros-Paredes, J., Vázquez-Semadeni, E., Gazol, A., 2011, MNRAS, 416, 1436
- Beuther, H., Linz, H., Tackenberg, J., et al., 2013, A&A, 553, 81
- Bohlin, R.C., Savage, B.D., Drake, J.F., 1978, ApJ 224, 132
- Butler, M., Tan, J., Kainulainen, J., 2014, ApJ, 782, L30
- Carey, S.J., Clark, F.O., Egan, M.P., et al., 1998, ApJ, 508, 721
- Carey, S., Feldman, P.A., Redman, R.O., et al., 2000, ApJ, 543, L157
- Contreras, Y., Schuller, F., Urquhart, J.S., et al., 2013, A&A, 549, 45
- Csengeri, T., Bontemps, S., Schneider, N., et al., 2011, A&A, 527, 135
- Csengeri, T., Urquhart, J.S., Schuller, F., et al., 2014, A&A, 565, 75
- Dempsey, J.T., Thomas, H.S., Currie, M.J., ApJS, 209, 1, 13
- Egan, M.P., Shipman, R.F., Price, S.D., et al., 1998, ApJ, 494, L199
- Federrath, C., Klessen, R.S., Schmidt, W., 2008a, ApJ, 688, L79
- Federrath, C., Glover, S., Klessen, R.S., 2008b, Physica Scripta, Volume 132, Issue , id. 014025
- Federrath, C., Klessen, R. S., 2013, ApJ, 763, 51
- Froebrich, D., Rowles, J., 2010, MNRAS, 406, 1350
- Girichidis, P., Konstandin, L., Whitworth, A.P., et al., 2014, ApJ, 781, 91
- Griffin, M., Abergel, A., Abreau, A., et al., 2010, A&A, 518, L3
- Henning, T., Linz, H., Krause, O., et al., 2010, 518, L95
- Hennemann, M., Motte, F., Schneider, N., et al., 2012, A&A, 543, L3
- Hill, T., Motte F., Didelon P., et al., 2011, A&A, 533, 94
- Jackson, J.M., Rathborne, J.M., Shah, R.Y., et al., 2006, ApJS, 163, 145
- Kainulainen, J., Beuther, H., Henning, T., & Plume, R., 2009, A&A, 508, L35
- Kainulainen, J., Alves, J., Beuther, H., et al., 2011a, A&A, 536, 48
- Kainulainen, J., Beuther, H., Banerjee, R., et al., 2011b, A&A, 530, 64
- Kainulainen, J., Tan, J.C., 2013, A&A, 549, 53
- Klessen, R. S., 2000, ApJ, 535, 869
- Kirk, H., Myers, P.C., Bourke, T.L., et al., 2013, ApJ, 766, 115
- Kritsuk, A.G., Norman, M.L., Padoan, P., Wagner, R., 2007, ApJ, 665, 416
- Kritsuk, A.G., Norman, M.L., Wagner, R., 2011, ApJ, 727, L20
- Lada, C.J., Lombardi, M., Alves, J., 2010, ApJ, 724, 687
- Lombardi, M., Lada, C., Alves, J., 2008, A&A, 489, 143
- Marston, A.P., Reach, W.T., Noriega-Crespo, A., et al., 2004, ApJS, 154, 333
- Molinari, S., Swinyard, B., Bally, J. et al. 2010, A&A, 518, L100
- Myers, P.C., Maradones, D., Tafalla, M., et al., 1996, ApJ, 465, L133
- Nguyen-Luong, Q., Motte, F., Hennemann, M., et al., A&A, 535, 76
- Padoan, P., Jones, J.T., Nordlund, A.A., 1997, ApJ, 474, 730
- Peretto, N., Fuller, G., 2010, ApJ, 723, 555
- Peretto, N., Fuller, G.A., Duarte-Cabral, A., et al., 2013, A&A, 555, 112
- Pilbratt, G., Riedinger, J., Passvogel, T., et al., 2010, A&A 518, L1
- Pillai, T., Wyrowski, F., Menten, K., et al., 2006, A&A, 447, 929
- Poglitsch, A., Waelkens, C., Geis, N., et al., 2010, A&A 518, L2
- Press, W.H., Teukolsky, S.A., Vetterling, W., Flannery, B.P., 1992, Cambridge University Press, 1992, 2nd ed., Chap. 14

- Rathborne, J.M., Jackson, J., Simon, R., 2006, *ApJ*, 641, 389
Rathborne, J.M., Garay, G., Jackson, J.M., et al., 2011, *ApJ*, 741, 120
Rathborne, J.M., Longmore, S., Jackson, J.M., et al., 2014, *ApJ*, in press, astro-ph:1409.0935
Roussel, H., 2013, *PASP*, 125, 1126
Roy, A., Martin, P., Polychroni, D., et al., 2013, *ApJ*, 763, 55
Russeil, D., Schneider, N., Anderson, L., et al., 2013, *A&A*, 554, 42
Sakai, T., Sakai, N., Foster, J.B., et al., 2013, *ApJ*, 775, 31
Schneider, N., Csengeri, T., Bontemps, S., et al., 2010, *A&A*, 520, 49
Schneider, N., Bontemps, S., Simon, R., et al., 2011, *A&A*, 529, 1
Schneider, N., Csengeri, T., Hennemann, M., et al., 2012, *A&A*, 540, L11
Schneider, N., André, Ph., Könyves, V., et al., 2013, *ApJ*, 766, L17
Schneider, N., Ossenkopf, V., Csengeri, T., et al., 2014, *A&A* submitted, astro-ph:1403.2996
Schuller, F., Menten, K., Contreras, Y., et al., 2009, *A&A*, 504, 415
Shipman, R.F., van der Tak, F.F.S., Wyrowski, F., et al., 2014, *A&A*, in press, astro-ph:1408.1515
Smith, R.J., Shetty, R., Stutz, A.M., Klessen, R.S., 2012, *ApJ*, 750, 64
Smith, R.J., Shetty, R., Beuther, H., Klessen, R.S., Bonnell, I.A., 2013, *ApJ*, 771, 24
Siringo, G., Kreysa, E., Kovacs, A., et al., 2009, *A&A*, 497, 945
Simon, R., Rathborne, J.M., Shah, R., et al., 2006a, *ApJ*, 653, 1325
Simon, R., Jackson, J.M., Rathborne, J.M., et al., 2006b, *ApJ*, 639, 227
Strong, J., Bloemen, J., Dame, T., et al., 1988, *A&A*, 207, 1
Tackenberg, J., Beuther, H., Henning, T., et al., 2014, *A&A*, 565, 101
Tafalla, M., Myers, P.C., Caselli, P., et al., 2002, *ApJ*, 569, 815
Teyssier, D., Hennebelle, P., Perault, M., 2002, *A&A*, 624, 638
Tremblin, P., Schneider, N., Minier, V., et al., 2014, *A&A*, 564, 106
Vazquez-Semadeni, E., Gonzales, R.F., Ballesteros-Paredes, J., et al., 2008, *MNRAS*, 390, 769
Walker, C.K., Narayanan, G., Boss, A.P., 1994, *ApJ*, 431, 767
Wang, K., Zhang, Q., Testi, L., et al., 2014, *MNRAS*, 439, 3275
Wang, Y., Zhang, Q., Pillai, T., et al., 2008, *ApJ*, 672, L33
Weiss, A., Neining, N., Hüttemeister, S., Klein, U., 2001, *A&A*, 365, 571
Zhang, Q., Wang, Y., Pillai, T., & Rathborne, J. 2009, *ApJ*, 696, 268

Appendix A: Herschel maps of infrared dark clouds

In this section, we show the whole sample of FIR-data from *Herschel* (70 μ m and 500 μ m data) and ATLASGAL (870 μ m), and column density and temperature maps obtained from SED-fits for the infrared dark clouds G11.11-0.12 ('snake'), G18.82-0.28 (Cloud A), and G28.53-0.25 (Cloud D). In addition, molecular line data maps (^{13}CO 1 \rightarrow 0 for G18.82-0.28 and G28.53-0.25, and ^{12}CO 3 \rightarrow 2 for G11.11-0.12) of the associated GMC are shown.

Appendix B: Probability distribution functions of column density for IRDCs

Probability distribution functions of column density, determined from *Herschel* data, for the infrared dark clouds G11.11-0.12 ('snake'), G18.82-0.28 (Cloud A), and G28.53-0.25 (Cloud D) are shown. The assumption of a constant line-of-sight temperature for each pixel affects the accuracy of the column density maps in massive, UV-illuminated GMCs with internal embedded (proto)stars, and can lead to an underestimation of the column density map. We carefully checked each SED fit for each pixel and found always very good fitting results. In addition, the IRDC we study here are not strongly affected by radiation, G28.53-0.25 is even not correlated with any protostellar object, so that we are confident in the validity of our column density maps.

Appendix C: KS-test

In order to verify if the column density distribution (PDF) we observed for G28.37+0.07 possibly arises from a lognormal distri-

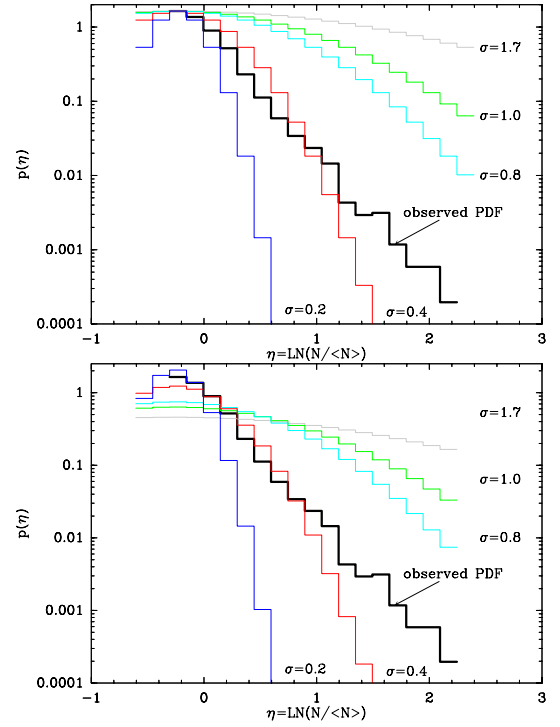


Fig. C.1. Synthetic distributions shown in various colors with different widths (indicated in the panel). The observed PDF for G28.37+0.07, constructed from *Herschel* data is indicated in bold black. The top panel shows distributions that are normalized to the peak, the bottom panel distributions that are normalized to the same number of pixels.

Table C.1. Results of KS-test. D and p are the parameters of the KS-test for the two normalizations (on peak value or number of pixels) used to generate the synthetic distributions.

PDF width σ	D_{peak}	p_{peak}	D_{integral}	p_{integral}
0.2	0.600	8.7843e-04	0.5790	1.7733e-03
0.4	0.301	2.8865e-01	0.3158	2.4667e-01
0.8	0.382	8.7724e-02	0.3684	1.1612e-01
1.0	0.579	1.4968e-03	0.4737	1.8105e-02
1.7	0.789	2.2829e-06	0.63158	4.6629e-04

bution, we performed a two-sample KS-test. We first generated synthetic functions following a lognormal distribution

$$p_{\eta} d\eta = \frac{1}{\sqrt{2\pi}\sigma^2} \exp\left[-\frac{(\eta - \mu)^2}{2\sigma^2}\right] d\eta \quad (\text{C.1})$$

where σ is the dispersion, i.e., the width of the distribution, η the mean logarithmic column density, and μ the peak (in units of η). In order to have a larger parameter space to compare, we varied σ between 0.2 and 1.7 (the latter is the width stated in KT).

For the normalization, we performed two approaches. First, we fixed the peak of all synthetic distributions to the observed value. The x-axis value for this peak at $A_{\nu} \sim 19$ ($\mu = -0.23$) was extracted from the PDF of the whole GMCs that revealed a log-normal + power-law tail distribution (Fig. 5). Because these distributions have the same peak value but not a normalization to the same number of pixels, we also produced a second set of functions that have such a normalization (but different peaks).

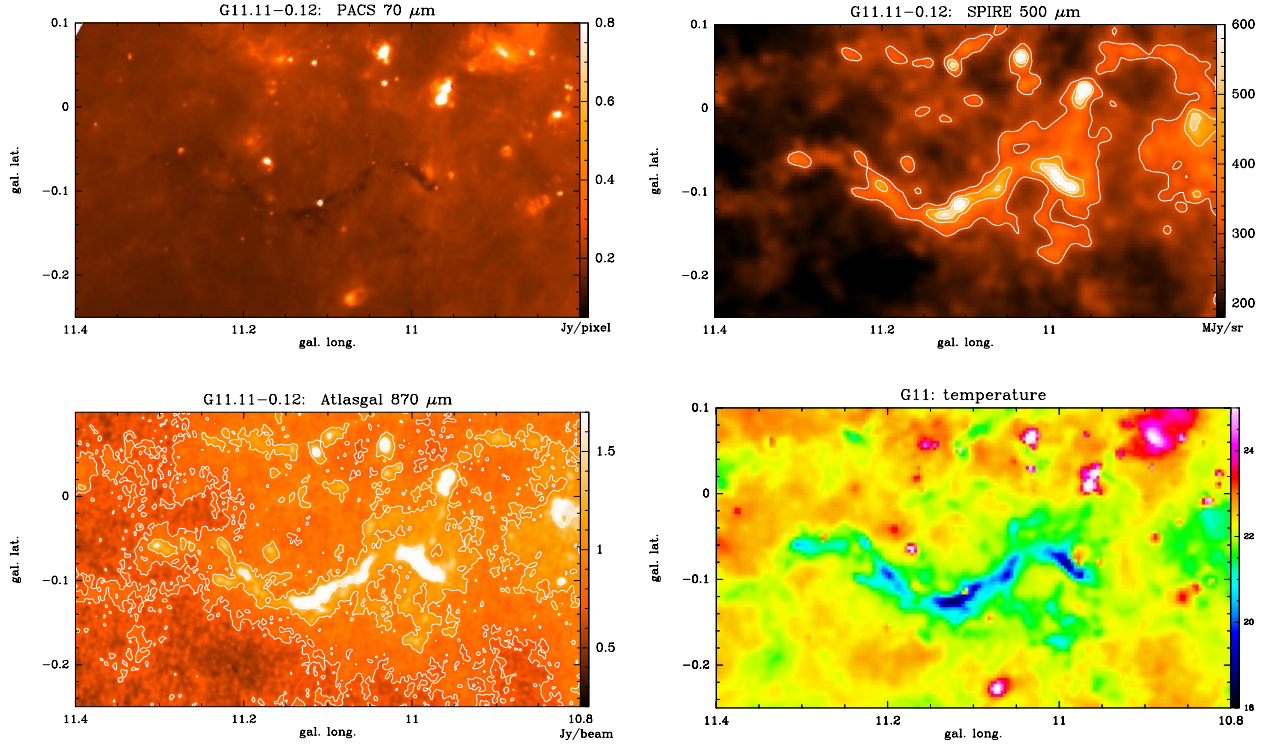


Fig. A.1. PACS 70 μm map, SPIRE 500 μm , and ATLASGAL 870 μm maps of G11.11-0.12 (the ‘snake’). The long filamentary structure is well visible as a dark (bright) feature in the 70 μm (500, 870 μm) maps. Bottom right: Temperature map from SED fit 160-500 μm .

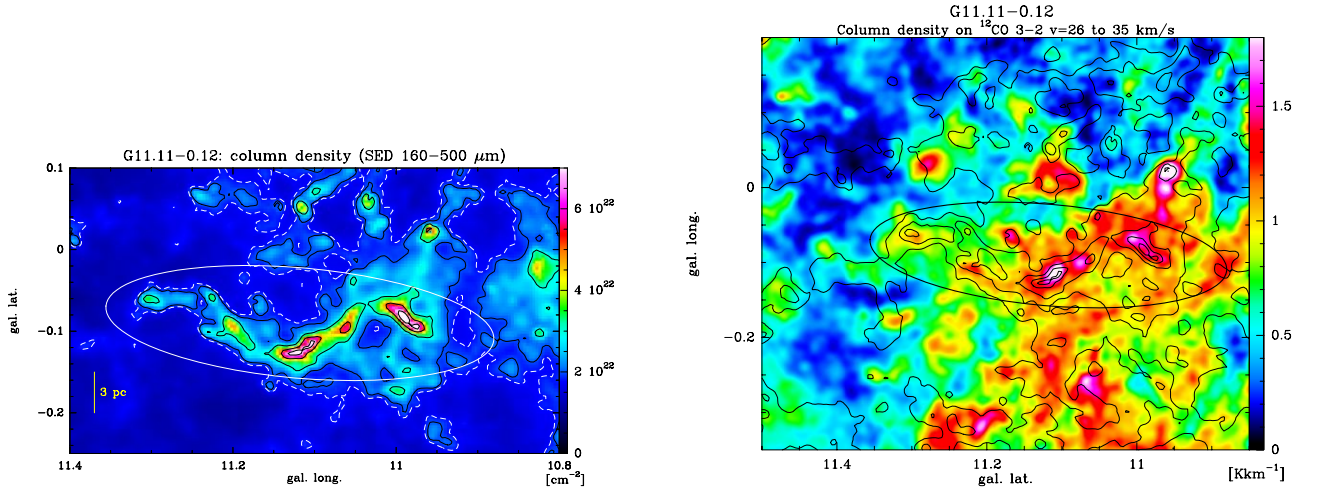


Fig. A.2. **Left:** Column density map of G11.11-0.12, obtained from SED-fit to *Herschel* 160, 250, 350, 500 μm data. The black contours indicate the levels $N_{\text{dust}}=2,3,5,7 \times 10^{22} \text{ cm}^{-2}$, the white dashed contour outlines the approximate completeness level, and the ellipse is taken from Simon et al. (2006b), defining the IRDC. **Right:** Line integrated ^{12}CO 3 \rightarrow 2 emission in color scale (in [K km/s]) between $v=26$ and 35 km s^{-1} , the velocity range of the bulk emission of G11.11-0.12 and the associated GMC. The *Herschel* H_2 column density is overlaid as black contours (levels $1.5, 2, 3, 5, 7 \times 10^{22} \text{ cm}^{-2}$) and the IRDC is outlined by an ellipse (Simon et al. 2006b).

Both sets of resulting synthetic distributions together with our observed one are shown in Fig. C.1.

Eye inspection only shows already that the observed PDF is not consistent with any lognormal distribution, in particular not with one of a large width ($\sigma=1.7$ was found in KT). To quantify this result, we give in Table C.1 the results of the two-sample KS-test, which gives the statistic and associated probability that two data sets are drawn from the same distribution. We performed the test using the IDL-routine ‘ksto.pro’ with the

algorithm taken from procedure of the same name in “Numerical Recipes” by Press et al. (1992). The parameter D gives the maximum deviation between the cumulative distribution of the observed PDF and the assumed underlying statistic (the lognormal in our case), while p shows the significance level of the KS-statistic. Small values of p – which is the case for our test – indicate that the pairwise distributions are significantly different. p -values below 0.3 show that we can exclude the scenario that our distribution can be fit with a lognormal distribution by more

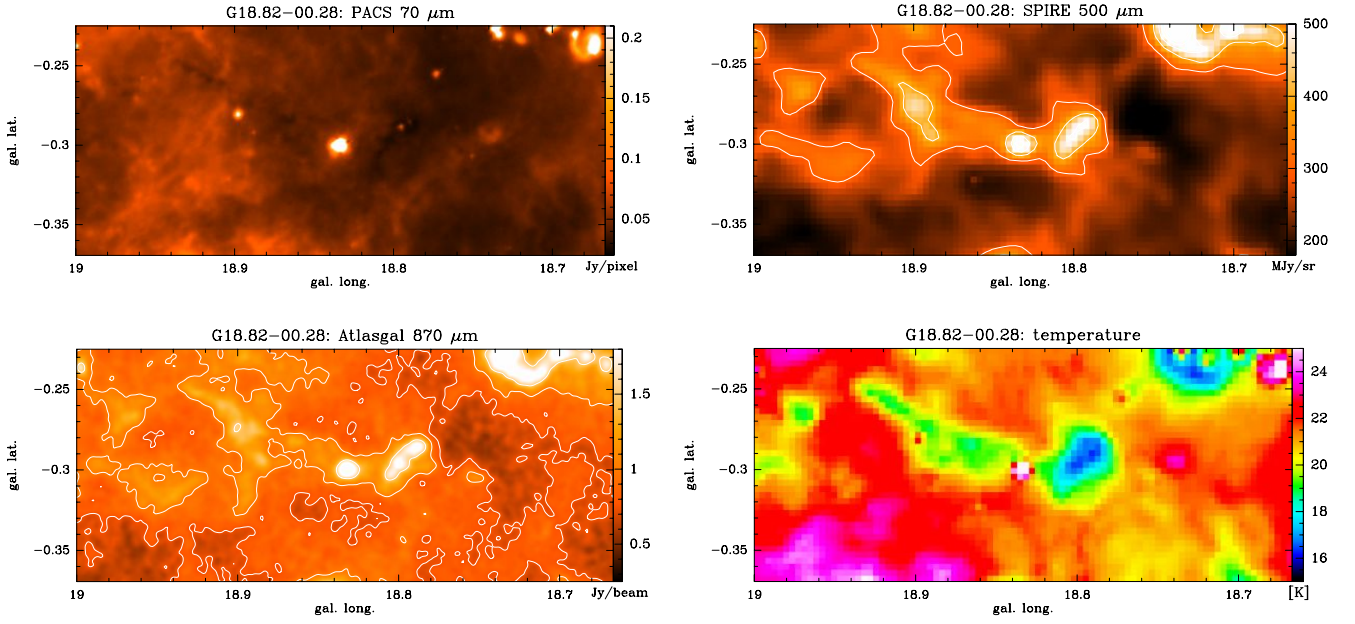


Fig. A.3. PACS 70 μm map, SPIRE 500 μm , and ATLASGAL 870 μm maps of IRDC G18.82-0.28 (Cloud A). The long filamentary structure is well visible as a dark (bright) feature in the 70 μm (500, 870 μm) maps. Bottom right: Temperature map from SED fit 160-500 μm .

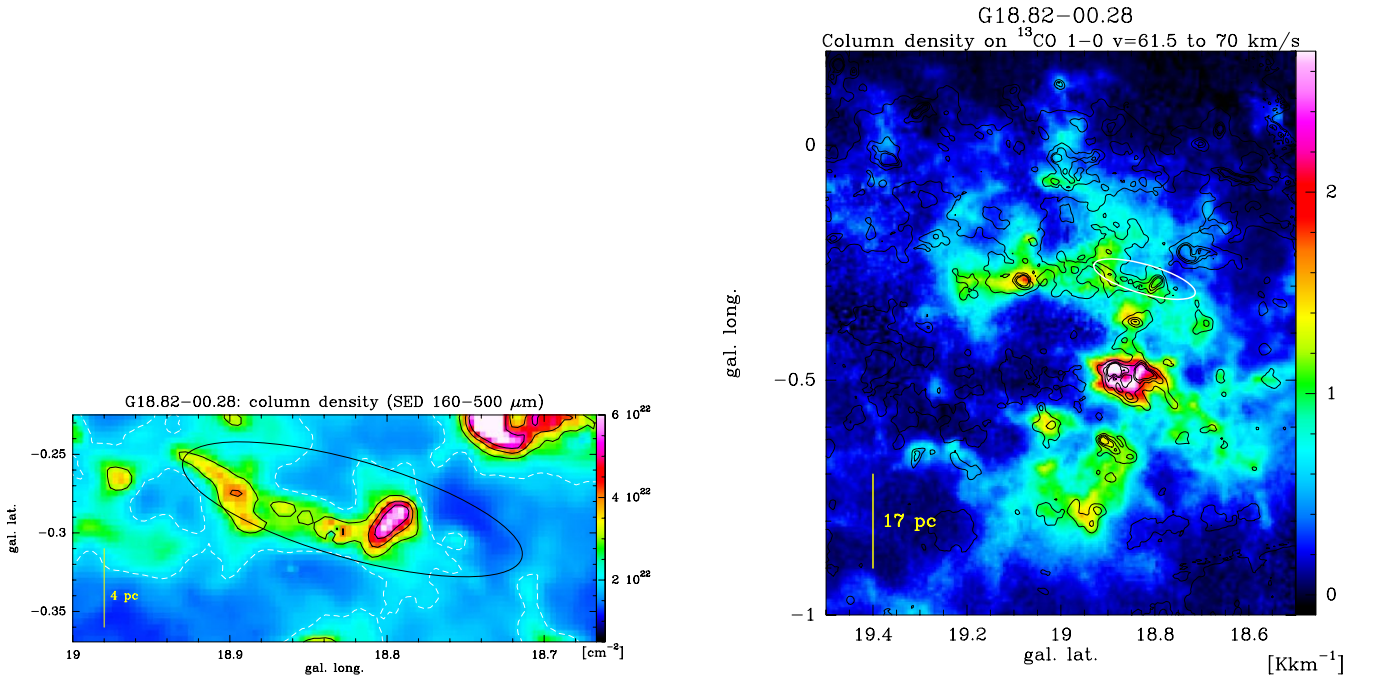


Fig. A.4. Left: Column density map of G18.82-0.28, obtained from SED-fit to *Herschel* 160, 250, 350, 500 μm data. The black contours indicate the levels $N_{\text{dust}}=2$ to $5 \times 10^{22} \text{ cm}^{-2}$ in steps of 10^{22} cm^{-2} , the white dashed contour outlines the approximate completeness level, and the ellipse is taken from Simon et al. (2006b), defining the IRDC. **Right:** Line integrated ^{13}CO 1 \rightarrow 0 emission in color scale (in $[\text{K km/s}]$) between $v=61$ and 70 km s^{-1} , the velocity range of the bulk emission of G18.82-0.28 and the associated GMC. Note that this GMC was already identified as a coherent cloud complex in Schuller et al. 2009. The *Herschel* H_2 column density is overlaid as black contours (levels 1,2,3,4,5 10^{22} cm^{-2}) and the IRDC is outlined by an ellipse (Simon et al. 2006b).

than one sigma. Note that though the pixel statistic is low and the binning is large, the general properties (width, peak, slope of power-law tail) of the PDF do not depend on binning in smaller or larger bins or varying the pixelsize/resolution (Schneider et al. 2014).

Appendix D: ^{12}CO 3 \rightarrow 2 spectra of G11.11-0.12

Figure D.1 shows ^{12}CO 3 \rightarrow 2 spectra at the location of some of the continuum sources of the IRDC G11.11-0.12 (no ^{13}CO data are available) in the velocity range where the emission is associated with the cloud. Similar as seen for G28.37+0.07, the opti-

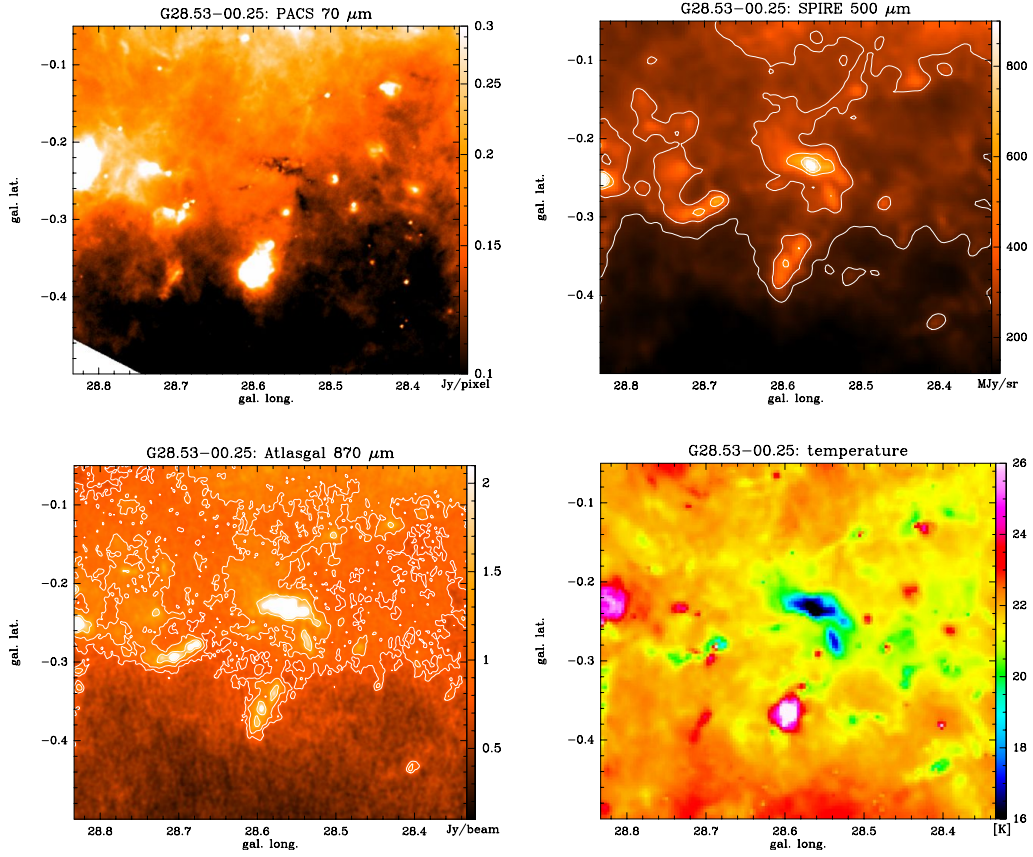


Fig. A.5. PACS 70 μm map (left), SPIRE 500 μm (middle) and ATLASGAL 870 μm maps of G28.53-0.25 (Cloud D). The long filamentary structure is well visible as a dark (bright) feature in the 70 μm (500, 870 μm) maps. Bottom right: Temperature map from SED fit 160-500 μm

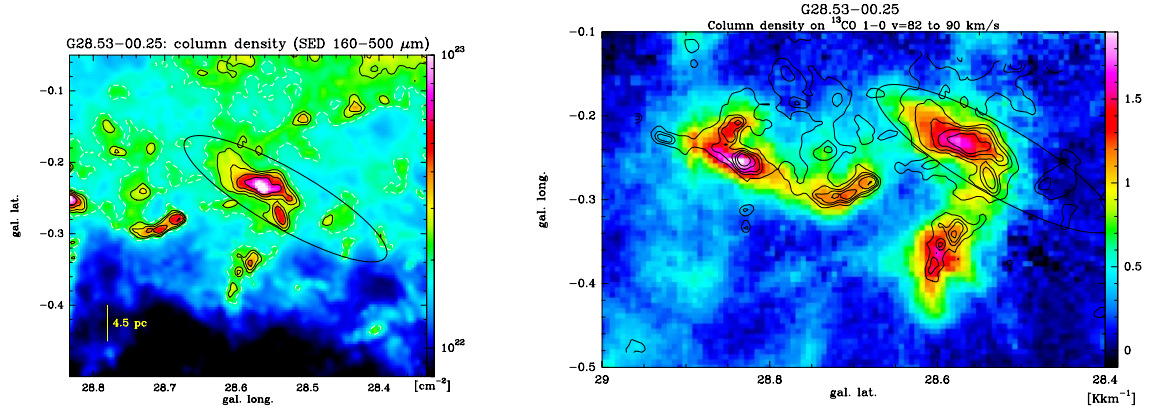


Fig. A.6. Left: Column density map of G28.53-0.25, obtained from SED-fit to *Herschel* 160, 250, 350, 500 μm data. The black contours indicate the levels $N_{\text{dust}}=2.5, 3, 4, 6 \times 10^{22} \text{ cm}^{-2}$, the white dashed contour outlines the approximate completeness level, and the ellipse is taken from Simon et al. (2006b), defining the IRDC. **Right:** Line integrated ^{13}CO 1 \rightarrow 0 emission in color scale (in [K km/s]) between $v=82$ and 90 km s^{-1} , the velocity range of the bulk emission of G28.53-0.25 and the associated GMC. The *Herschel* H_2 column density is overlaid as black contours (levels 2, 2.5, 3, 4, 6 10^{22} cm^{-2}) and the IRDC is outlined by an ellipse (Simon et al. 2006b).

cally thick ^{12}CO line shows a self-absorbed dip close to the velocity of the optically thin N_2H^+ line (indicated by a blue dashed line). Note that the velocity resolution of the CO data is only 1 km s^{-1} while the one of N_2H^+ is 0.2 km s^{-1} so that resolution effects can play a role. The most straightforward explanation for the observed profile is infall, i.e. a line shape cause by the radial inward motion of gas onto a central source.

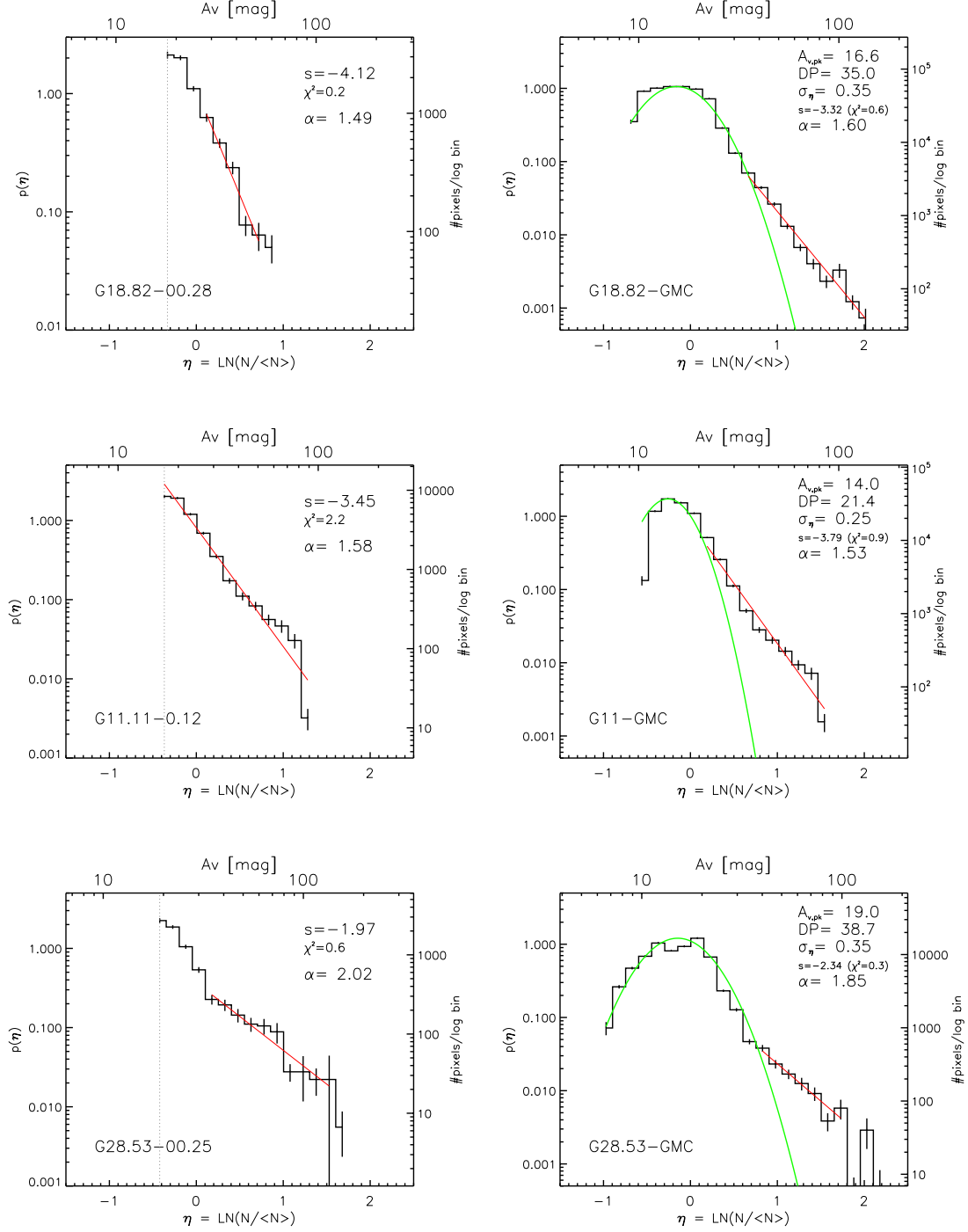


Fig. B.1. PDFs derived from *Herschel* column density maps (SED fit using only the *Herschel* wavelengths 160, 250, 350, and 500 μm) at 36'' angular resolution. The left panel shows the PDFs of pixels comprising only the IRDC, i.e., G18.82-0.28 (Cloud A), G28.53-0.25 (Cloud D), and G11.11-0.12. The right panel shows the PDFs from the associated GMC, including the IRDC. The left y-axis gives the normalised probability $p(\eta)$, the right y-axis the number of pixels per log bin. The upper x-axis is the visual extinction and the lower x-axis the logarithm of the normalised column density. The dashed vertical line indicates the completeness level. The red line is a power-law fit to the high column density tail (linear regression). The lower limit for the fit is determined by the turnover point between lognormal and power-law distribution seen in the PDFs of the GMC. Inside each panel, the slope s of the fit and the exponent α of an equivalent spherical density distribution are indicated.

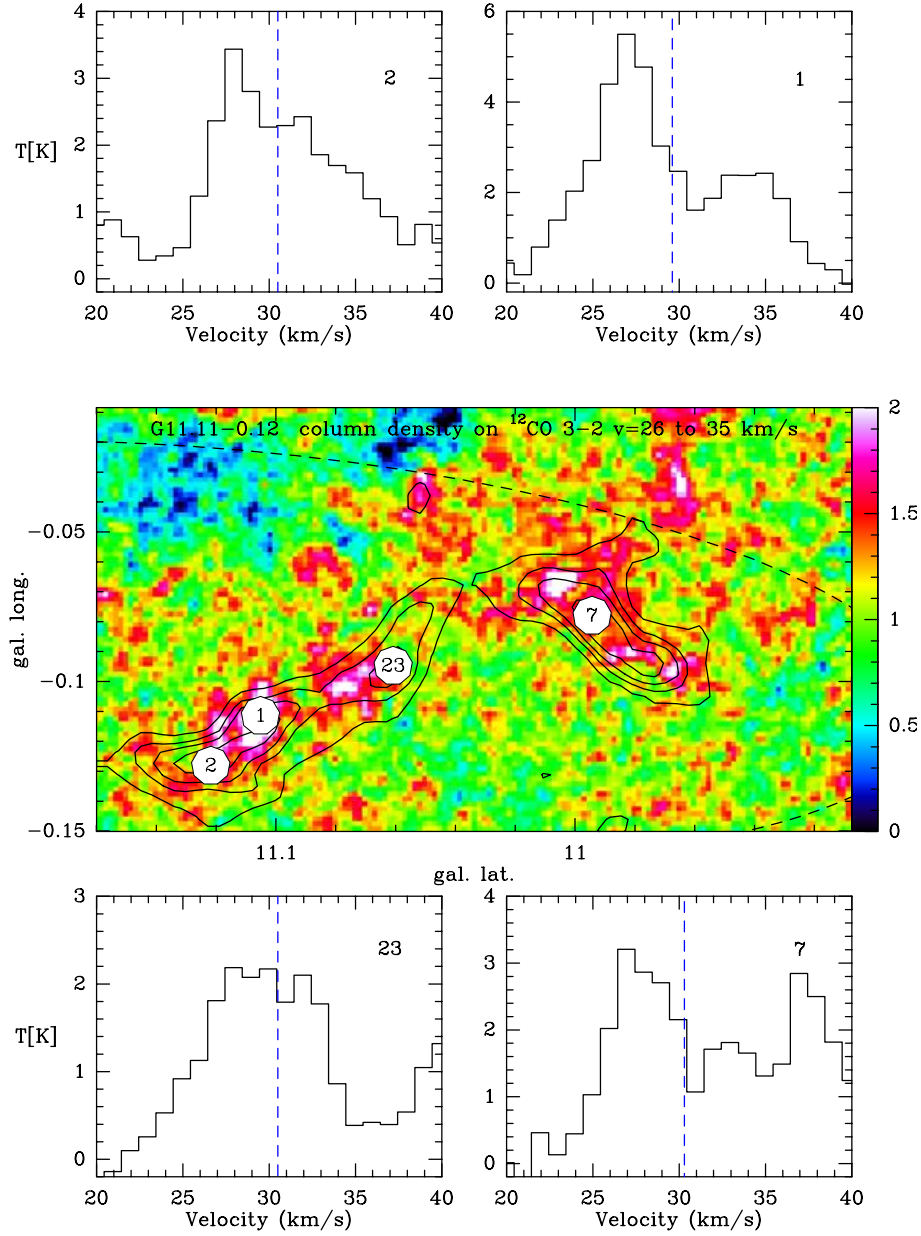


Fig. D.1. The middle panel shows in color the line integrated ^{12}CO 3 \rightarrow 2 emission (between 26 and 35 km s $^{-1}$) of G11-0.12. The dust column density from *Herschel* is overlaid as black contours (levels 3, 4, 5, 6 10^{22} cm $^{-2}$). The numbering from 1 to 4 indicates the position of submm-continuum sources detected with ATLASGAL and subsequently observed in N_2H^+ (Tackenberg et al. 2014). The ^{12}CO 3 \rightarrow 2 spectra at these positions are displayed in the panels around. The blue dashed line denotes the center velocity of the N_2H^+ line.